1D Imaging of Central Loop Transient Electromagnetic Soundings

by

Niels B. Christensen
Aarhus University, Department of Earth Sciences, Laboratory of Geophysics

ABSTRACT

The success of geophysical investigations in general is to a large extent determined by the density of the measurements and the quality of the interpretations. The development in geophysical data acquisition has gone in the direction of covering larger and larger areas with more and more dense grids of measurements. This development has been especially pronounced in the field of transient electromagnetic data acquisition (TEM) for mineral prospecting, where airborne systems collect large volumes of data, and also in the field of environmental geophysics, where dense measurements of transient soundings have proved very useful in connection with hydrogeological investigations.

An ordinary 1D least squares iterative inversion of TEM sounding, data requires that the interpreter supply an initial model, and the computation time is not at all negligible even on present-day computing platforms. With a large daily production of soundings this procedure is slow, and there is need for fast approximate ways of interpretation.

This paper outlines the development of an algorithm for imaging of TEM soundings in the central loop configuration based on the Born approximation and the Frechet kernel for the step response of the vertical magnetic dipole. The Frechet kernel depends on the resistivity of the halfspace, but instead of using one Frechet kernel for a certain halfspace resistivity for all data, the Frechet kernel is scaled according to the all-time apparent resistivity of the measurements at every delay time. In this way, the actual resistivity structure of the halfspace is taken into account, and the inversion problem is linearized resulting in better imaged models.

The imaging procedure produces models with 20-40 layers which fit the original data, typically within 5-10%. No initial model is required, and the algorithm is therefore well suited for automatic inversion. The algorithm makes it possible to see the results of a day's work in a matter of minutes and to implement on-line inversion simultaneous with the measurements.

Introduction

The transient electromagnetic sounding method has found increased use for a variety of purposes during the last two decades.

Within the field of mineral prospecting, the use of large-scale, high-current instrumentation for deep penetration has been supplemented with airborne systems well-suited for covering large areas with profile lines of transient measurements (Macnae et al., 1991). Recent instrumentation will measure with a density of one sounding per 10 meters, resulting in hundreds of soundings per minutes to be interpreted.

In the last decade, small portable instruments have been developed, which, working with small currents and short turn-off times, are applicable for general geological mapping of the near-surface geology. Transient electromagnetic soundings are now routinely used in connection with environmental geophysical investigations such as hydrogeological investigations, prospecting for raw materials, and mapping of dump sites and waste deposits (Fittermann and Stewart, 1986; Buselli, et al., 1990; Hoekstra and Blohm, 1990; Christensen and Soerensen, 1994).

In Denmark, transient electromagnetic soundings have become one of the standard methods of large-scale hydrogeological investigations. This is due to the ability of transient measurements to delineate good conductors like clay and salt water, which constitute the effective lower boundaries of freshwater resources. The strategy of application has been to obtain coverage of the target area with transient soundings with a density of approximately 16-25 per km^2 often along profile lines. The success of transient sounding in hydrogeological investigations has led to the development of pulled-array transient electromagnetic equipment (PA-TEM), where a transmitter loop and a continuously measuring receiver coil are towed through the landscape (Soerensen, et al., 1995). With the PA-TEM method, the density of transient soundings will be as high as for airborne measurements.

Traditionally, transient soundings have been interpreted with 1D earth models with few layers (2-6), and though the efficiency of the least squares iterative inversion programs has improved and the speed of commonly available computers has increased, it is still time-consuming to interpret tran-

JEEG, v. 0, no. 1 (July 1995), p. 53-66

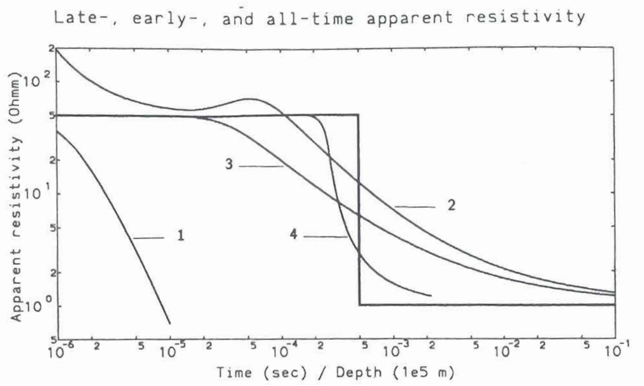

Figure 1. Apparent resistivity transforms for a 2-layer descending model with resistivity 100 Ωm in the first layer, 10 Ωm in the second layer, and 50m layer thickness. The true model is shown with the thick grey curve. (1) the impulse response early time apparent resistivity, (2) the impulse response late-time apparent resistivity, (3) the step response all-time apparent resistivity, (4) the step response all-time apparent resistivity plotted as a function of diffusion depth.

sient soundings. In the case of airborne surveys and PA-TEM measurements, it is not feasible to invert the whole set of data using ordinary 1D least squares iterative inversion programs, and an "imaging" algorithm for fast approximate interpretation becomes interesting. The computer-based design of modern transient instruments also makes it desirable to develop fast interpretation techniques, which can be used for on-line interpretation in the field, and thus assist the field crew in deciding about the location of future measurements.

The term "imaging" has become widely used in the geophysical literature to denote fast interpretation algorithms for geophysical measurements, and many papers have been published about the subject (Macnae and Lamontagne, 1987; Nekut, 1987; Eaton and Hohmann 1989). Polzer (1985) developed an imaging algorithm based on a delay-time formulation of the forward transient problem. Recently, Smith et al., (1994) published a paper on the use of the Frechet kernel in developing an imaging algorithm for coincident loop soundings.

In the following, an imaging algorithm based on the Frechet kernel of the step response of the vertical magnetic dipole and the all-time apparent resistivity transform shall be developed and used in connection with central loop transient measurements.

Apparent Resistivity Transforms

The use of the apparent resistivity transform and the plot of apparent resistivity as a function of time may be regarded as a sort of "zero order" imaging procedure: it is fast, and it gives a first qualitative understanding of the resistivity variation with depth. For impulse-response data, which are by far the most commonly measured data, the apparent resistivity is not uniquely defined (Spies and Eggers, 1986). There are two unambiguous definitions of apparent resistivity: one valid for early times, and one valid for late times; most often the late, time apparent resistivity definition is used. However, the late, time apparent resistivity suffers from a number of drawbacks. It is not correct at early times, but always has a descending branch, and the curve exhibits under- and overshoot when the resistivity of the subsurface changes. For these reasons, the usefulness of the late-time apparent resistivity transform for impulse data is limited, and only very experienced interpreters can estimate subsurface resistivity from an immediate inspection of the curve.

The early-time apparent resistivity transform is only of use in cases where the diffusion of the current system in the ground is in the early stage. If not, the early-time apparent resistivity transform fails to describe accurately any portion of the curve as it decreases rapidly with time.

The situation is different when considering the step response. For the step response from central loop soundings, it is possible to uniquely define an apparent resistivity, which is valid for all times. This all-time apparent resistivity is defined through the expression for the step response of the homogeneous halfspace (Ward and Hohmann, 1987)

$$H_z = \frac{I}{2a}\left[\frac{3}{\sqrt{\pi}\,\theta a}\exp(-\theta^2 a^2) + \left(1 - \frac{3}{2\theta^2 a^2}\right)\operatorname{erf}(\theta a)\right], \qquad \theta = \sqrt{\frac{\mu\sigma}{4t}}, \tag{1}$$

where σ is conductivity, μ is the permeability, a is the radius of the circular transmitter loop, and t is time.

The normalized response $2aH_z/I$, which only attains values in the interval from zero to unity, is a monotonically increasing function of the parameter combination (θa). For any 1D earth model, the normalized response will lie in the interval from zero to unity, and there is exactly one inverse solution for θa. The apparent resistivity is then determined by

$$\rho_a = \frac{\mu a^2}{4t(\theta a)^2}. \tag{2}$$

This all-time apparent resistivity does not have the spurious character of the impulse response late-time apparent resistivity. The all-time apparent resistivity of a homogeneous halfspace is in fact a constant equal to the resistivity of the halfspace. For layered models, there is no under- and overshoot, and the step response all-time apparent resistivity has a smooth transition when the subsurface resistivity changes. It is thus much easier to infer the resistivity distribution from this resistivity transform. Figure 1 illustrates the behavior of the early, the late, and the all-time apparent resistivity transforms for a 2-layer descending model.

Although the step response all-time apparent resistivity gives a qualitative picture of the resistivity variation in the subsurface, it is a very smoothed version of the subsur-

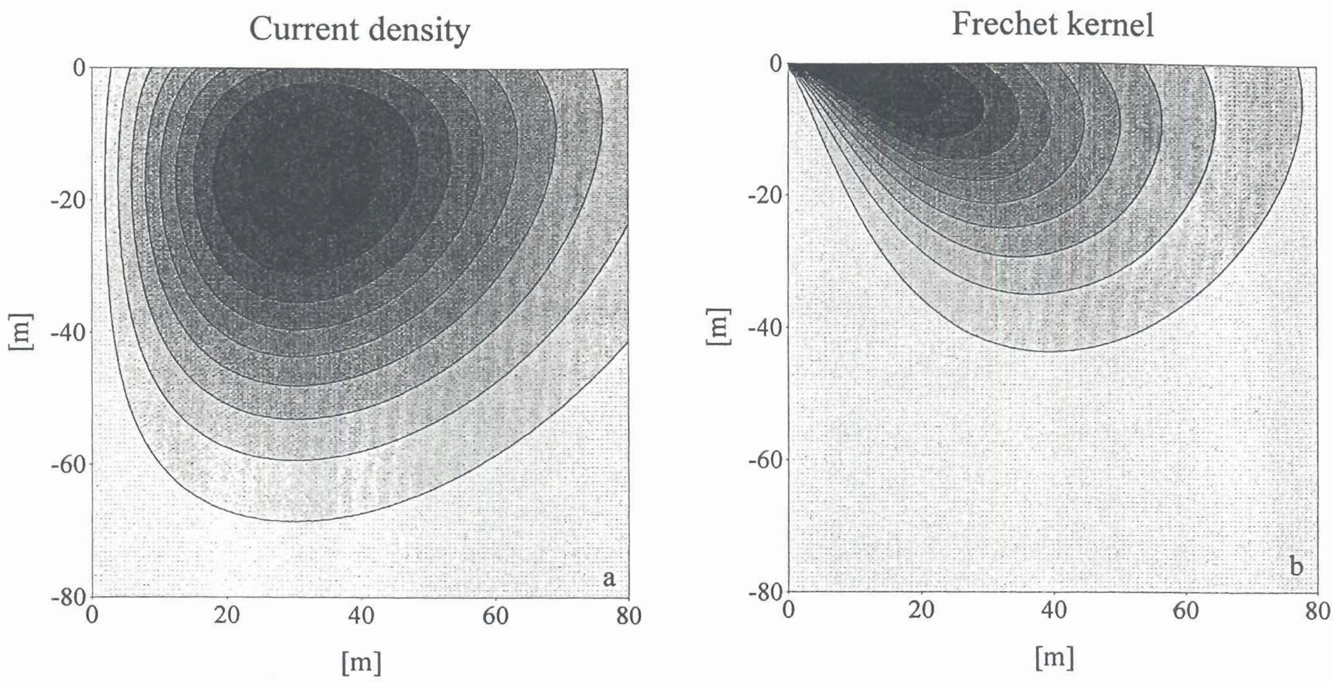

Figure 2. Figure 2a is a contoured plot of the current density in the ground 500 μs after turnoff of a vertical magnetic dipole on a 1m halfspace. In fig. 2b, the current density is weighted according to its contribution to the vertical magnetic field at the center. Contour interval is 10% of the maximum value. The plot window covers 80 x 80m.

face resistivity. What we would like is a "sharpening up" of the apparent resistivity curve to look more like the true resistivity distribution in the ground. This involves an association of depth with each measurement. It is this sharpening procedure which is most often called imaging.

It is interesting to notice that plotting the step response all-time apparent resistivity as a function not of time, but of diffusion depth, gives a surprisingly better result in terms of similarity with the true resistivity distribution. For a homogeneous halfspace, the diffusion depth, d, is defined as

$$d = \sqrt{\frac{2t}{\mu\sigma}} \quad , \qquad (3)$$

where t is time, μ is the magnetic permeability, and σ is the conductivity of the halfspace.

Having found the step response all-time apparent resistivity as a function of time, $\rho a(t)$, we may define the diffusion depth for our measured data as

$$d = \sqrt{\frac{2t\rho_a(t)}{\mu}} \quad , \qquad (4)$$

and plotting $\rho a(d)=\rho a(d(t,\rho a(t)))$ in a double logarithmic plot gives a simple imaging procedure with virtually no computational cost. The step response all-time apparent resistivity as a function of diffusion depth is also seen in fig. 1. The reason this simple plotting convention works so well is that the diffusion depth is a measure of the depth to the maximum current density and thereby also, to some extent, to the depth of maximum sensitivity. The all-time apparent resistivity can be considered as a sort of average resistivity of the subsurface within the volume, where the current system prevails, and it thus reflects the history of the diffusion process. By using the all-time apparent resistivity in the formula for the diffusion depth, the actual resistivity structure of the subsurface is taken into account.

Current Distribution and Sensitivity Function

To gain a better understanding of the underlying physics of transient measurements, let us consider the transient response of a vertical magnetic dipole source. Many authors have shown plots of the current distribution as a function of time in a homogeneous halfspace, the so called "smoke ring". This current distribution, resulting from a step-off at time zero, is shown in fig. 2a. The current in the ground has only an azimuthal component, and the current maximum diffuses outwards and downwards with time, while the maximum broadens and decreases in amplitude due to ohmic loss in the conductor. The current density maximum follows a straight line, making an angle of 30° with the surface. It must be noted that the current density at the surface is approximately 75% of the current maximum at depth at all times. The picture illustrates how the sensitivity of the transient sounding method to the resistivity distribution moves downwards and outwards with time.

The sensitivity of the transient method, however, does not depend directly on the current distribution at depth, but on the effect of the current distribution on the measured field;

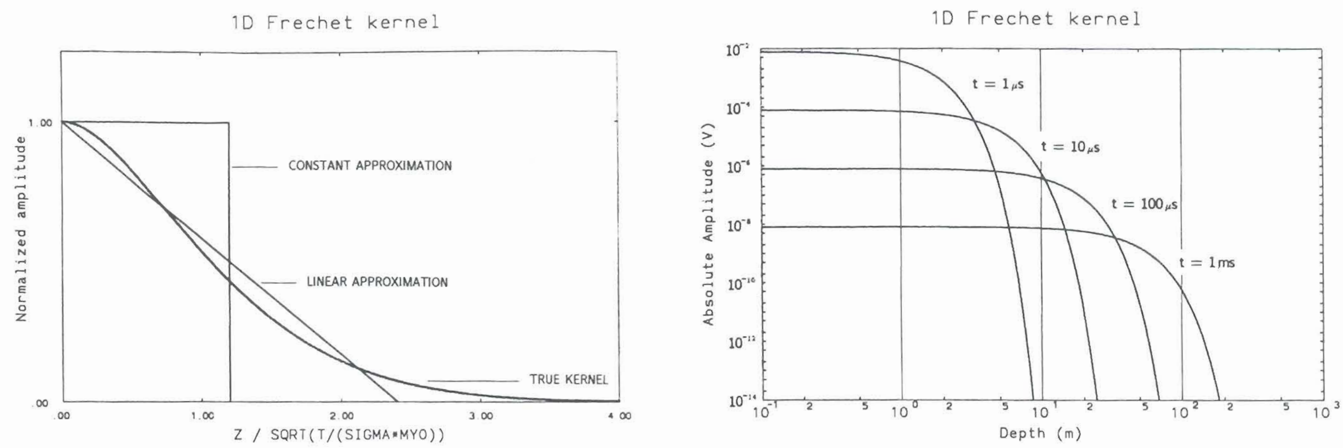

Figure 3. Figure 3a shows the normalized 1D Frechet kernel for the transient vertical magnetic dipole in the case of a homogeneous halfspace as a function of normalized depth. The constant and the linear approximations to the Frechet kernel are also shown. Figure 3b shows the unnormalized Frechet kernel for a halfspace resistivity of 1 Ωm at the times 1μs, 10μs, 100μs, and 1ms in a double logarithmic plot.

in our case, the vertical magnetic field was measured at the source point. Using the usual formula for the magnetic field on the axis of a circular current element situated at the point with the cylindrical coordinates (r,z), the current element contributes to the magnetic field at the surface as

$$dH(\sigma,t) = j(\sigma,t,r,z)\, dr\, dz \times \frac{1}{2} \frac{r^2}{(r^2+z^2)^{3/2}} , \qquad (5)$$

where σ is the conductivity, t is time, and $j(\sigma,t,r,z)$ is the current density at (r,z).

Figure 2b shows the current distribution of fig. 2a weighted according to its contribution to the magnetic field. This plot reveals some interesting features of the transient method. At all times, the sensitivity stays high at the surface close to the center, and can be described as a cone-shaped structure, which broadens outwards and downwards with time. The maximum follows a straight line making an angle of 20 with the surface. Note also that there is almost no sensitivity to the resistivity distribution within a cone with an opening angle of 30 directly under the source. This has consequences for the way we intuitively think about the physics of diffusion and should also be taken into account in connection with 2D and 3D modelling.

In the quasi-stationary case, which is the one considered here, the function described in fig. 2b is the 2D (or 3D rotationally symmetric) sensitivity function of the magnetic field with respect to conductivity for the homogeneous halfspace referring to an annulus-shaped model element. The Frechet kernel is identical to this function divided with the conductivity, of the halfspace.

The 1D Frechet Kernel

The 1D Frechet kernel for a layered earth structure can be found by integrating the 3D Frechet kernel over r from 0 to ∞. This results in an analytic expression (see appendix A)

$$F(\sigma,t,z) = \frac{M}{4\pi} \frac{1}{16\,\sigma\,\tau^4} \mathcal{F}(u) , \qquad (6)$$

where

$$\mathcal{F}(u) = \left\{ \frac{2u}{\sqrt{\pi}} (2u^2+1) e^{-u^2} - (4u^4+4u^2-1)\,\mathrm{erfc}(u) \right\} , \qquad (7)$$

$$u = \frac{z}{2\tau} ,$$

σ is the conductivity of the halfspace,
M is the magnetic moment of the dipole, and

$$\tau = \sqrt{\frac{t}{\mu\sigma}} .$$

Using the expression for the magnetic field from a vertical magnetic dipole

$$H = \frac{M}{30} \left(\frac{\mu\sigma}{\pi t}\right)^{\frac{3}{2}} = \frac{M}{30\,\pi^{3/2}\,\tau^3} , \qquad (8)$$

the Frechet kernel can be expressed as

$$F(\sigma,t,z) = \frac{1}{\sigma} H\, \mathcal{F}'(u) , \qquad (9)$$

where

$$\mathcal{F}'(u) = \frac{15\sqrt{\pi}}{32\,\tau} \mathcal{F}(u), \quad \int_0^\infty \mathcal{F}'(u)\, dz = 1 . \qquad (10)$$

Figure 3a shows a normalized plot of $F(\sigma,t)$ in a linear coordinate system. It is seen that the sensitivity is a bell-shaped function of u (and thereby of z), which has its maximum at the surface at all times. The double logarithmic plot of $F(\sigma,t)$ at four different times seen in fig. 3b, shows how the Frechet kernel expands downwards with time while the amplitude decreases and the sensitivity drops very abruptly to zero with depth, decreasing as u^{-3}exo($-u^2$) (see appendix A).

The Imaging Algorithm

The imaging algorithm proposed here is based on the following considerations:

1) From the measurements, we can find the all-time apparent resistivity based on the step response.
2) The Frechet kernel for any 1D model can be approximated by that of the homogeneous halfspace in the sense that the shape of the kernel is the same, but the depth to which it has diffused at a certain time depends on the actual resistivity structure. This depth of diffusion is taken as that of the homogeneous halfspace with a resistivity equal to the all-time apparent resistivity of the actual model at the given time.
3) The imaging algorithm developed for the vertical magnetic dipole case can be used for central loop sounding data.

1) The field quantity most often measured with transient equipment is the impulse-response. However, given impulse response data, we may calculate the step response numerically (see appendix B). From the step response we can calculate the all-time apparent resistivity as a function of time.
2) These assumptions are the critical points of the procedure and the main idea of this algorithm. However, it is justified by the observation that the Frechet kernel of inductive electromagnetic methods is not very model-dependent (Boerner and Holladay, 1990). As seen above, plotting the all-time apparent resistivity as a function of diffusion depth is, in itself, quite a successful imaging procedure, and this makes it natural to try and scale the diffusion of the Frechet kernel according to the all-time apparent resistivity. Eventually, as far as an imaging algorithm is concerned, the ultimate justification lies in the fact that it works.
3) This is obviously the case for late times. For early times, it is a good approximation if the time is not too early, the resistivity is not too low, and the radius of the loop not too large. However, central loop magnetic field data are not directly used. The imaging algorithm to be developed will be expressed in terms of the all-time apparent conductivity. This transformation removes a significant part of the influence of the geometry of the actual configuration, if the transformation from magnetic field to all-time apparent resistivity is done with the correct circular loop transmitter formula for the transmitter loop in question. This is illustrated in fig. 4, where all-time apparent resistivity curves for 2-layer increasing and decreasing models have been calculated. For decreasing models, the maximum difference at time 5μs is 7.1% and for increasing models the maximum difference at time 5μs is 2.4%. Most impulse-response systems would not measure earlier than that, and topsoil resistivities lower than 10Ω are not very common except in saline/arid regions. For all the models of fig. 5, the all-time apparent resistivity transform for a central loop configuration and for the vertical magnetic dipole configuration are identical.

The Frechet Kernel Inverse

In the Born approximation, valid for small conductivity changes, the Frechet kernel describes the change in the response as a linear functional of the change in subsurface conductivity:

$$H(t_i) \simeq H^{ref}(t_i) + \int_0^\infty F\left(\sigma^{ref}(z), t_i, z\right)\left(\sigma(z) - \sigma^{ref}(z)\right) dz \quad , (11)$$

where (t_i) is the measured magnetic field at the time t_i.
$H^{ref}t_i$ is the magnetic field of the reference model.
$F(\sigma^{ref}(z),t,z)$ is the Frechet kernel of the reference model.
$\sigma(z)$ is the conductivity of the subsurface.
σ^{ref} is the conductivity of the reference model.

The response of the homogeneous halfspace with conductivity σ_0 is the integral of the Frechet kernel multiplied with conductivity (eq. 9)

$$H^0(t_i) = \int_0^\infty F(\sigma_0, t_i, z)\, \sigma_0 \, dz = \frac{M}{30}\left(\frac{\sigma_0 \mu}{\pi t}\right)^{3/2} , \qquad (12)$$

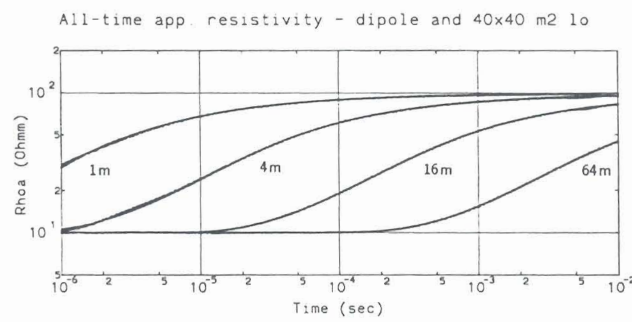

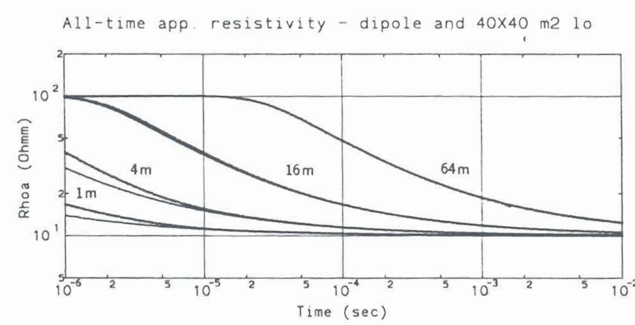

Figure 4. Comparison between all-time apparent resistivity curves for a magnetic dipole (thin black curves) and a square 40 x 40 m² loop (thick grey curves) for a series of a) increasing and b) decreasing 2-layer models. In fig. a) the top layer resistivity is 10 Ωm, the resistivity of the second layer is 100 Ωm, and the layer thicknesses are 1m, 4m, 16m, and 64m. In fig. b) the top layer resistivity is 100 Ωm, the resistivity of the second layer is 10 Ωm, and the layer thicknesses are 1m, 4m, 16m, and 64m.

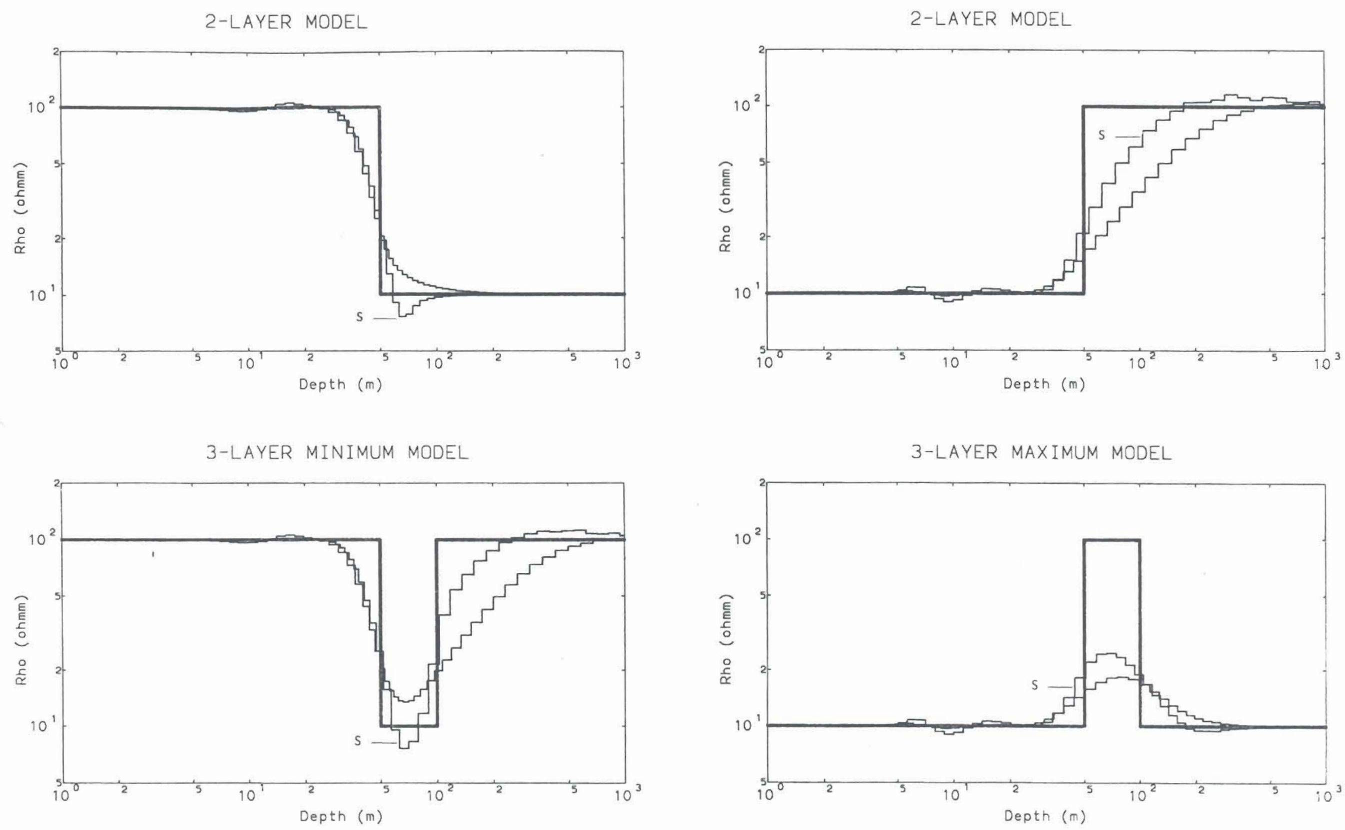

Figure 5. The models obtained using the imaging procedures on 40 x 40 m² central loop soundings. The fig. shows a comparison between the results obtained with the more damped constant approximation and the more sensitive linear approximation to the Frechet kernel for four models: two 2-layer models (descending and ascending) and two 3-layer models (minimum and maximum). The true models are shown with thick grey curves. The more sensitive inverse is marked with an "S".

so in the case where the reference model is a homogeneous halfspace, we find

$$H(t_i) \simeq H^0(t_i) + \int_0^\infty F(\sigma_0, t_i, z)\,(\sigma(z) - \sigma_0)\,dz$$

$$= \int_0^\infty F(\sigma_0, t_i, z)\,\sigma(z)\,dz \;. \tag{13}$$

This expression shows that the Frechet kernel can be used in an "absolute" sense and not just in a differential sense as in eq. (11).

For a layered 1D structure with L layers given by the layer boundaries $z_j, j=1, L+1, z_1=0, z_{L+1}=\infty$ we find that by generalizing the previous expression and utilizing the assumption 2)

$$H(t_i) = \sum_{j=1}^{L} \sigma_j \int_{z_j}^{z_{j+1}} F(\sigma_a(t_i), t_i, z)\,dz$$

$$= \sum_{j=1}^{L} \sigma_j \left\{ \hat{F}(\sigma_a(t_i), t_i, z_{j+1}) - \hat{F}(\sigma_a(t_i), t_i, z_j) \right\} , \tag{14}$$

where $\sigma a(t_i)$ is the all-time apparent conductivity at the time t_i and $\hat{F}$ is the integral of the Frechet kernel, which can be expressed analytically (see appendix A):

$$\hat{F}(\sigma, t, z) = \frac{M}{4\pi} \frac{1}{120\,\sigma\,\tau^3} \times \hat{\mathfrak{F}}(u)$$

$$\hat{\mathfrak{F}}(u) = \left\{ \frac{2}{\sqrt{\pi}} (6u^4 + 7u^2 - 8)\,e^{-u^2} - u\,(12u^4 + 20u^2 - 15)\,\mathrm{erfc}(u) \right\} . \tag{15}$$

Using the expression (8) for the magnetic field H, the integrated Frechet kernel can be expressed as

$$\hat{F}(\sigma, t, z) = \frac{H}{\sigma} \times \hat{\mathfrak{F}}'(u) \;, \tag{16}$$

where

$$\hat{\mathfrak{F}}'(u) = \frac{\sqrt{\pi}}{16} \times \hat{\mathfrak{F}}(u) \;, \quad \hat{\mathfrak{F}}'(\infty) - \hat{\mathfrak{F}}'(0) = 1 \tag{17}$$

Introducing the expression (16) into the imaging formula (14) finally gives us an imaging formula, which involves the all-time apparent conductivity and not the magnetic field itself

$$H(t_i) = \sum_{j=1}^{L} \sigma_j \left\{ \hat{F}(\sigma_a(t_i), t_i, z_{j+1}) - \hat{F}(\sigma_a(t_i), t_i, z_j) \right\}$$

$$= \sum_{j=1}^{L} \sigma_j \left\{ \frac{H(t_i)}{\sigma_{a(t_i)}} \hat{\mathcal{F}}'(\sigma_a(t_i), t_i, z_{j+1}) - \frac{H(t_i)}{\sigma_{a(t_i)}} \hat{\mathcal{F}}'(\sigma_a(t_i), t_i, z_j) \right\} \Rightarrow$$

$$\sigma_a(t_i) = \sum_{j=1}^{L} \sigma_j \left\{ \hat{\mathcal{F}}'(\sigma_a(t_i), t_i, z_{j+1}) - \hat{\mathcal{F}}'(\sigma_a(t_i), t_i, z_j) \right\} . \tag{18}$$

Equation (18) expresses the apparent conductivity as a weighted sum of the conductivities of each layer.

Approximations to the Frechet Kernel

Using the exact Frechet kernel in the inverse formulation (18) results in imaged resistivity models displaying wild excursions, and conventional damping schemes do not prevent the oscillatory behavior. By introducing general weight matrices, these oscillations can normally be damped. However, instead of this elaborate harnessing of the inverse problem, we shall investigate the possibilities of using a family of simple, piecewise linear approximations which show a surprisingly well-behaved and predictable performance and which lead to an even faster inversion.

The simplest approximation to the Frechet kernel is to set it equal to a constant down to a certain depth under which it is zero. The constant is taken as the surface value, and the depth, which in this context shall be called the diffusion limit, is determined so that the integral of the Frechet kernel from zero depth to infinity is correct, i.e. identical to that of the true kernel. The approximation is justified by the observation that the Frechet kernel decreases extremely rapidly with depth (as $u^{-3}\exp(-u^2)$). This approximation is equivalent to saying that what is measured with transient soundings is the conductance of the subsurface down to the diffusion limit. Figure 3a shows the analytical Frechet kernel together with the constant approximation and the linear approximation, which shall be investigated later in this paragraph.

The constant approximation to the Frechet kernel is given by

$$F(\sigma,t,z) = F_0 = \frac{M}{4\pi} \frac{1}{16\sigma\tau^4} = H(t) \cdot \frac{15\sqrt{\pi}}{32\tau} \frac{1}{\sigma} \quad \text{for } z \le z^D ,$$

$$F(\sigma,t,z) = 0 \quad \text{for } z > z^D , \tag{19}$$

where $H(t_i)$ is the value of the magnetic field at time t_i, and the diffusion limit of the Frechet kernel z^D is determined by

$$z^D \times \frac{M}{4\pi} \frac{1}{16\tau^4} = H(\sigma,t) = \frac{M}{30\pi^{3/2}} \frac{1}{\tau^3} \quad \Rightarrow \quad z^D = \frac{32}{15\sqrt{\pi}} \tau . \tag{20}$$

The expression (19) for the Frechet kernel can be used together with the imaging formula (18) for any layered earth model, but choosing the layer boundaries z_j equal to the diffusion limits of the Frechet kernel, z^D, results in a very simple system of equations, as equation (18) reduces to

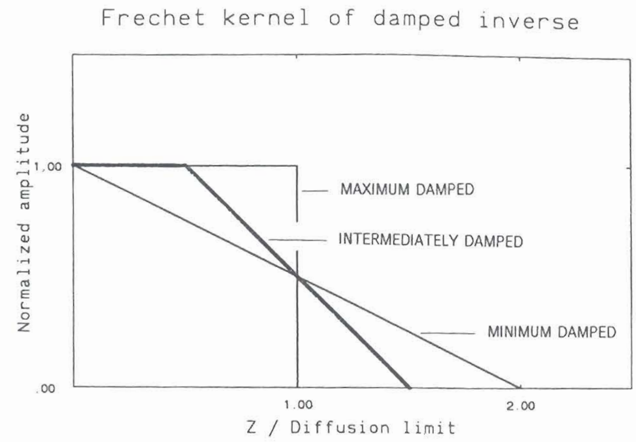

Figure 6. The Frechet kernel of the intermediately-damped inverse (thick grey curve) shown together with the constant approximation (maximum-damped) and the linear approximation (minimum-damped).

$$\sigma_i^a = \sum_{j=1}^{i} \sigma_j \frac{h_j}{z_i^D} , \tag{21}$$

where h_j is the thickness if the j'th layer. Since $z_i^D = \sum_{j=1}^{i} h_j$, equation (21) expresses the apparent conductivity as a weighted sum of the conductivities of each layer with the layer thicknesses as weight factors.

The system of linear equations (21) may easily be inverted for the layer conductivities by forward substitution, as the matrix involved is lower triangular. The inversion procedure is a sort of "stripping the earth" algorithm.

Another approximation to the Frechet kernel is obtained by taking a linear function as the approximating function. Utilizing the results from the constant approximation, we immediately find

$$F(\sigma,t,z) = \frac{M}{4\pi} \frac{1}{16\sigma\tau^4} \left(1 - \frac{z}{2z_D}\right)$$

$$= H(t) \cdot \frac{15\sqrt{\pi}}{32\tau} \frac{1}{\sigma} \left(1 - \frac{z}{2z_D}\right) \quad \text{for } z \le 2z^D , \tag{22}$$

$$F(\sigma,t,z) = 0 \quad \text{for } z > 2z^D .$$

Also, in the case of the linear approximation to the Frechet kernel, the layer boundaries shall be defined equal to the diffusion limits, which are now $2z^D$. This results in a system of equations in which the matrix is lower triangular and the system is solved through substitution.

In fig. 5, a number of results are gathered for four different models: two 2-layer models (descending and ascending) and a maximum and a minimum 3-layer model. The performance of the imaging algorithms for the doubly descending and the doubly descending 3-layer models are simi-

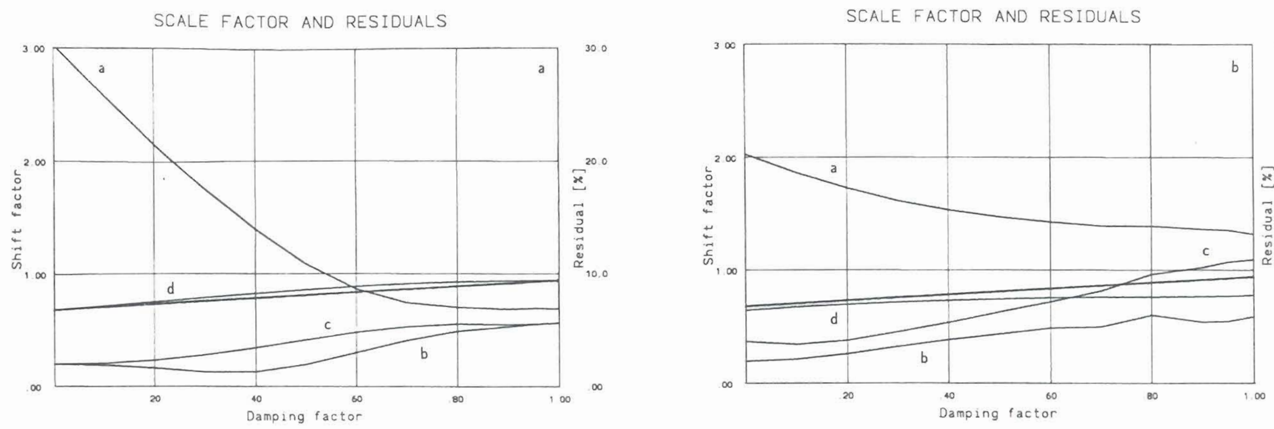

Figure 7. Scaling factors for the diffusion depths and residuals of the 2-layer models of fig. 5. Figure 7a shows the residuals of the unshifted model (a), the optimally-shifted model (b), and the suboptimally shifted model (c) for the descending case. Also the scaling factor for the diffusion limit is shown (d) together with a linear approximation to it (thick grey curve). Figure 7b shows the analogous curves for the ascending 2-layer model of fig. 5.

lar to those for the 2-layer models. The models resulting from the application of the imaging algorithms for the constant and the linear approximation to the Frechet kernel on synthetic noise-free data are shown together with the true resistivity models. It is seen that the imaging algorithms work very well with descending type models, but react slower to ascending resistivity models. The worst performance is seen with the maximum model, which is to be expected. From the asymptotic behavior, it is seen that the imaged models reach the true value of the resistivity very well. For the constant approximation there is practically no undershoot and overshoot in the imaged models, while the linear approximation exhibit a little overshoot and undershoot. Both approximations represent a damped inverse, but while the constant approximation is a well-damped inverse, the linear approximation results is a more sensitive. The linear approximation results in models closer to the true models. It has a steeper ascent for ascending models, and for the 3-layer minimum model the linear approximation results in a more well defined region of low resistivity and the resistivity of the 2nd layer of the imaged model is closer to the true value than is the case for the constant approximation.

Both inverse procedures work satisfactorily on perfect magnetic field data. However, when noise is added to the magnetic field values, i.e. when real measurements are considered, the question of controlling the damping becomes important. To be able to adjust the damping of the inverse continuously between the extremes of the constant and the linear approximation, we shall consider an intermediate piecewise linear approximation illustrated in fig. 6. The figure shows approximations, which are constant down to a certain depth and linear down to the diffusion limit, constructed in such a way as to keep the integral of the approximate Frechet kernel unchanged. The approximation is given by

$$
\begin{aligned}
F(\sigma,t,z) &= A && \text{for} \quad z' < \tfrac{\alpha}{2}\,, \\
F(\sigma,t,z) &= A\left\{1-\tfrac{1}{2}\,\frac{2z'-\alpha}{1-\alpha}\right\}, \quad z' = z/D && \text{for} \quad \tfrac{\alpha}{2} < z' < 1-\tfrac{\alpha}{2}\,, \\
F(\sigma,t,z) &= 0 && \text{for} \quad 1-\tfrac{\alpha}{2} < z'\,,
\end{aligned}
\tag{23}
$$

where α is a damping factor between zero (linear approximation) and unity (constant approximation), and the amplitude A and the diffusion limit D are given by

$$A = F_0 \text{ and } D = 2z_D\,. \tag{24}$$

Choosing the layer boundaries z_j according to

$$z_j = (1 - \tfrac{1}{2}\alpha)\, D_j \quad , \tag{25}$$

results in a linear system of equations with a lower triangular matrix solved by substitution.

The parameter can be chosen continuously between 0 and 1, corresponding to the linear and the constant approximation to the Frechet kernel respectively. This enables the damping to be adjusted to the noise level of the data. The chosen damping should be strong enough to give reasonable models without wild excursions and small enough to allow as many features of the model as possible to become visible. Because of the rapid back substitution technique of solving the linear system of equations, the imaging procedure is as fast as the click of the mouse, and different damping parameters can be tried out practically without computational cost.

Fine Tuning of the Inverse

The above derivations are founded upon the assumption that the diffusion of the Frechet kernel is adequately described by the all-time apparent resistivity. Whether or not this is the case can be judged from the misfit between the model responses of the imaged models and the original data.

Figure 7a shows the misfit in percent between the model response of the imaged models and the original magnetic field data for the descending 2-layer curve of fig. 5. For small damping factors, the misfit is rather large with a residual of 30% for the undamped linear approximation. Increasing the damping causes the residual to decrease to a level around 7% for the most damped case (the constant approximation). This can, however, be remedied by introducing a shift of the imaged models towards smaller depths to the layer boundaries. Whereas the integral of the Frechet kernel must be kept correct to obtain the right imaged resistivity values, a simultaneous scaling of the diffusion limit and the amplitude with a certain factor, keeping the integral constant, will result in a scaling of the depths ascribed to the imaged resistivity with that same factor. Figure 7a shows the optimal shift of the diffusion limit as a function of the damping coefficient and the resulting residual for the imaged models. As expected, the residual is now lower for the undamped inverse than for the most damped inverse. The residuals are 2-5%, which means that the imaged models are essentially correct, and it shows that the imaging algorithm is in effect a very good linearization of the inverse problem. Choosing a linear approximation to the shift as a function of the damping factor, which is also shown in fig. 7a, results in suboptimal residuals not very much greater than the optimal ones.

Figure 7b shows a similar analysis for the 2-layer ascending model of fig. 5. In this case the optimal shift is somewhat smaller, and the residuals of the optimally-shifted models are 2-7%, again a very good inverse. Using the linear approximation to the shift as a function of damping factor of the descending model results in suboptimal residuals about twice as large. Considering the characteristic of transient soundings to give a very good resolution of the depth to a good conductor, it seems reasonable to put more emphasis on the correct determination of this depth than on the correct depth to a bad conductor, and consequently choose the shift according to the descending model. The shift factor for the diffusion limit found in this pragmatic way can be expressed as

$$\text{shift factor} = 0.67821 + 0.26068 \cdot \alpha \qquad (26)$$

The models of Figure 5 have all been subjected to this shift.

Application of the Imaging Procedure to Field Measurements

Figure 8 illustrates the application of the imaging algorithm to a profile of transient soundings in the central loop configuration. The well-damped inverse of the constant approximation to the Frechet kernel has been used and the result is displayed in fig. 8a as a contoured model section. The

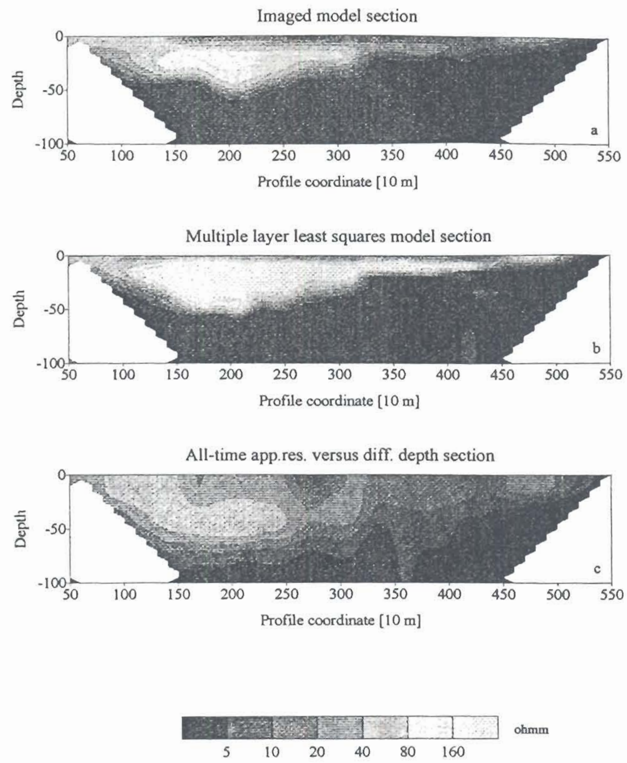

Figure 8. Imaged model sections from a TEM profile for the detection of the salt water horizon on the island of Romo in Denmark. The section of fig. 8a is based on the imaging algorithm, section 8b shows the results of least squares inversion with multiple-layer models, and fig. 8c is a section of all-time apparent resistivity as a function of diffusion depth.

profile consisting of 17 soundings is from the island of R|m|, Denmark, where it transects the NE corner of the island. The depth to the good conductor, the saltwater horizon, is small at the ends of the profile where the distance to the coast is small; and larger in the middle of the profile situated further inland. Besides the depth to the salt water, fig. 8 also shows the varying surface resistivities along the profile.

The same profile has been interpreted with the 1D least squares iterative inversion program SELMA (Christensen and Auken, 1992) with multiple-layer models consisting of 15-20 layers. In the inversion the layer boundaries have been kept fixed. The models resulting from the least squares inversion are shown as a contoured model section in fig. 8b. Essentially the models sections of figs. 8a and 8b are identical.

To illustrate that the imaging algorithm developed here is superior to the plotting of all-time apparent resistivity as a function of diffusion depth, a contoured section based on the simple plotting convention of equation (4) is presented in fig. 8c.

The next example, shown in fig. 9, is from a hydrogeological investigation around Gjern River 30 km west

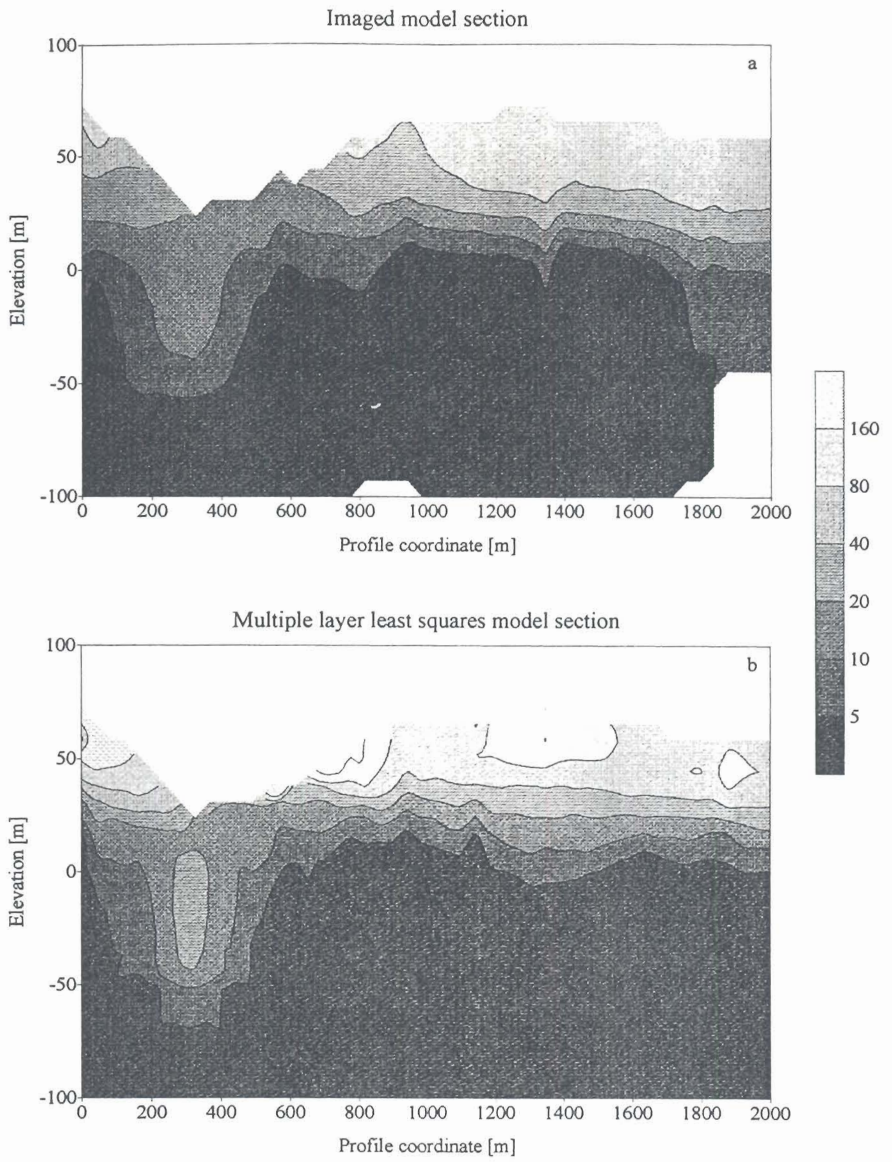

Figure 9. Imaged model sections from a TEM profile for the mapping of the deeper parts of the Gjern River Valley, Denmark. The section of fig. 9a is based on the imaging algorithm, while section 9b shows the results of least squares inversion with multiple-layer models.

of Aarhus, Denmark. The riverbed follows a straight line for many kilometers, which has given rise to speculations about tectonic movements as a cause for this unusual behavior. A series of profiles of transient soundings were placed across the river valley, one of which is presented in fig. 9. The imaged model section based on 18 soundings is presented together with a section obtained through rigorous least squares inversion with multiple-layer models with fixed-layer boundaries. In both sections a depression in the well conducting basement consisting of heavy Tertiary clay is seen directly under the river valley supporting the assumption of tectonic movements as a cause for the morphology of the valley. In the section based on least squares inversion, the surface-near high resistivities are higher than in the imaged section. This is to be expected, since the imaging algorithm is based on the Born approximation which does not quite reproduce larger resistivity contrasts.

Discussion and Conclusions

The algorithm outlined here has some similarities with the work of Smith et al., (1994) and with the work of Polzer (1985).

Smith et al., (1994) developed an imaging algorithm for coincident loop soundings using the Frechet kernel and the impulse-response apparent resistivity. The apparent resistivity was ascribed a depth equal to the depth of the maximum of the Frechet kernel. A linearized inversion with a boxcar averring function was also described, but the use of the impulse-response apparent resistivity instead of the step-response apparent resistivity used here gave erratic models, when overshoot and undershoot was present in the impulse-apparent resistivity curves.

Polzer (1985) considered time as a function of the magnetic field and developed a theory for inversion of the arrival-time data of a certain amplitude of the magnetic field. Using a linear approximation to the Frechet kernel a one-step imaging inverse was developed, where the diffusion depth was scaled according to the arrival time of a reference model, a homogeneous halfspace. This scaling of the arrival-time Frechet kernel can be shown to be completely equivalent to the scaling according to all-time apparent resistivity presented here and results in similar-imaged models.

The present approach to imaging of transient electromagnetic data using the Born approximation and a Frechet kernel scaled not only with the time of the measurement, but also with the all-time apparent resistivity, has proved itself to be an efficient procedure for fast interpretation of transient soundings. Choosing the layer boundaries of the model equal to the diffusion depths results in a lower triangular linear system of equations which is solved very rapidly. The imaging algorithm is fast, robust, fully-automated, and requires no initial model. The damping of the inverse procedure can be controlled by the choice of approximation to the Frechet kernel.

The model sections obtained through the imaging procedure are in very good agreement with model sections based on rigorous least squares inversion.

The imaged models can be used directly to give an overview of an area, and contoured model sections based on imaged models from soundings along profile lines give a very fast insight into the subsurface conductivity distribution.

The imaged models can be used as good input models to an iterative least squares inversion program.

The simplicity and speed of the imaging algorithm makes it an attractive choice for an on-line interpretation procedure in modern computerized transient data acquisition systems.

Besides giving an efficient imaging procedure, the present study also casts new light on the nature of transient measurements and has resulted in a deeper understanding of the dynamics of current diffusion associated with transient loop sources.

The approach of finding the step response from the impulse response through a least squares formulation seems a viable one.

The scaling of the Frechet kernel according to some parameter of the reference model, for which a sort of "instantaneous" or "apparent" value can be given, is a principle which is applicable in many other inverse problems. In electromagnetic induction problems, in general, the Frechet kernel for the homogeneous halfspace depends on the halfspace resistivity, and if a sort of apparent resistivity can be defined, the procedure outlined here for the transient case should be applicable. It would be very interesting to see the approach applied to the MT case. In the case of low-induction number measurements and for direct current problems, the Frechet kernel of the homogeneous halfspace is independent on halfspace resistivity, and the above procedure cannot be used. In the case of thermal conduction, a similar approach should be viable.

Acknowledgments. I would like to thank Professor James Macnae for fruitful discussion during my stay at the CRCAMET in January and February 1995 as well as Keeva Vozoff for critical comments to the manuscript. Also my colleagues at home have contributed with valuable critical comments. Thanks also to Lena Macnae for helping make my English more English.

References

Abramowitz, M., and Stegun, I.A., 1964, Handbook of mathematical functions, Dover Publications, Inc, New York, ninth printing.

Boerner, D.E., and Holladay, J.S., 1990, Approximate Frechet derivatives in inductive electromagnetic soundings, Geophysics, **55**, 1589-1595.

Buselli, G., et al., 1990, Detection of groundwater contamination near waste disposal sites with transient electromagnetic and electrical methods, in Geotechnical and Environmental Geophysics, Vol. **2**, Environmental and groundwater, Ward, S.H., Ed, SEG Investigations in geophysics, no. 5, 27-39.

Christensen, N.B., 1990, Optimized Fast Hankel Transform filters, Geophys. Prosp., **38**, 545-568.

Christensen, N.B., and Auken, E., 1992, Simultaneous electromagnetic layered model analysis: Proceedings of the Interdisciplinary Inversion Workshop 1, Aarhus 1992, Jacobsen, B.H. Ed, GeoSkrifter **41**, 49-56.

Christensen, N.B., and Soerensen, K.I., 1994, Integrated use of electromagnetic methods for hydrogeological investigations: Proceedings of the Symposium on the Application of Geophysics to Engineering and Environmental Problems, Boston, March 1994, p 163-176.

Eaton, P.A., and Hohmann, G.W., 1989, A rapid inversion technique for transient electromagnetic soundings, Phys. Earth Plan. Int., **53**, 384-404.

Erdelyi, A., Magnus, W., Oberhettinger, F., and Tricomi, F.G., 1954, Tables of integral transforms, McGraw-Hill Book Company, Inc.

Fittermann, D.V., and Stewart, M.T., 1986, Transient electromagnetic sounding for groundwater, Geophysics, **51**, 995-1005.

Gradshteyn, I.S., and Ryzhik, I.M., 1965, Table of integrals, series, and products, Academic press, fourth edition.

Hoekstra, P., and Blohm, M.W., 1990, Case histories of time-domain electromagnetic soundings in environmental geophysics, in Geotechnical and environmental geophysics, Vol. **2**, Environmental and groundwater, Ward, S.H., Ed, SEG Investigations in geophysics, no. 5.

Johansen, H.K., and Soerensen, K.I., 1979, Fast Hankel Transforms, Geophys. Prosp., 27, 876-901.

Macnae, J.C., and Lamontagne, Y., 1987, Imaging quasi-layered conductive structures by simple processing of transient electromagnetic data, Geophysics, **52**, 545-554.

Macnae, J.C., Smith, R.S., Polzer, B.D., Lamontagne, Y., and Klinkert, P.S., 1991, Conductivity-depth imaging of airborne electromagnetic step-response data, Geophysics, **56**, 102-114.

Nekut, A.G., 1987, Direct inversion of time-domain electromagnetic data, Geophysics, 52, 1431-1435.

Polzer, B.D., 1985, The interpretation of inductive transient magnetic sounding data, Research in Applied Geophysics No. 36, Geophysics Laboratory, Department of Physics, University of Toronto.

Smith, R.S., Edwards, R.N., and Buselli, G., 1994, An automatic technique for presentation of coincident-loop, impulse-response, transient, electromagnetic data, Geophysics, 59, 1542-1550.

Spies, B.R., and Eggers, D.E., 1986, The use and misuse of apparent resistivity in electromagnetic methods, Geophysics, 51, 1462-1471.

Soerensen, K.I., Effersoe, F., and Christensen, A.J., 1995, Pulled array transient electromagnetic method (PA-TEM): Proceedings of the Symposium on the Application of Geophysics to Engineering and Environmental Problems, Orlando, Florida, 899-903.

Ward, S.H., and Hohmann, G.W., 1987, Electromagnetic theory for geophysical applications, in Electromagnetic methods in applied geophysics, Vol.1, Nabighian, M.N., Ed, SEG Investigations in geophysics, no. 3, 285-426.

APPENDIX A
THE FRECHET KERNEL

In this appendix, an analytical expression for the Frechet kernel of the step response of the vertical magnetic dipole over a homogeneous halfspace shall be developed.

Let us consider the electric field, and thereby the current, in a homogeneous halfspace from a vertical magnetic dipole in the quasi-stationary approximation. First, we observe that the transient currents in a conductivity structure, which is a function of depth only, is in horizontal circles. The electric field in the azimuthal direction is given by Ward and Hohmann (1987, 4.49),

$$E_\theta(\underline{r},t) = -\frac{M\mu}{2\pi}\int_{-\infty}^{\infty} \exp(i2\pi ft)\left[\int_0^{\infty} \frac{i\omega \exp(-\alpha_1 z)}{\lambda+\alpha_1}\lambda^2 J_1(\lambda r)\, d\lambda\right] df \;, \quad \text{(A-1)}$$

where

M is the moment of the dipole,
μ is the magnetic susceptibility of empty space,
f is the frequency,
t is the time,

$$\alpha_1 = \sqrt{\lambda^2+i\omega\mu\sigma} \quad , \quad \omega = 2\pi f$$

σ is the conductivity of the halfspace,
J_1 is the Bessel functions of order 1.

The Fourier Transform of the step response

$$\Phi'(\lambda,z,t) = \int_{-\infty}^{\infty} \frac{\exp(-\alpha_1 z)}{\lambda+\alpha_1}\exp(i2\pi ft)\, df \;, \quad \text{(A-2)}$$

may be evaluated explicitly by expressing it as an inverse Laplace Transform

$$\Phi'(\lambda,z,t) = \frac{1}{\sqrt{\mu\sigma}}\exp\left(-\frac{\lambda^2}{\mu\sigma}t\right)$$

$$\cdot\frac{1}{2\pi i}\int_{\beta-i\infty}^{\beta+i\infty} \frac{\exp(-z\sqrt{\mu\sigma u})}{\frac{\lambda}{\sqrt{\mu\sigma}}+\sqrt{u}}\exp(ut)\, du \;,\; \beta = \frac{\lambda^2}{\mu\sigma} \quad \text{(A-3)}$$

which is given by Erdelyi, et al., (1954, page 246 (12)),

$$\Phi'(\lambda,z,t) = \frac{1}{\mu\sigma}\exp(\lambda z)\left\{\frac{1}{\sqrt{\pi}\,\tau}\exp\left[-\left(\lambda\tau+\frac{z}{2\tau}\right)^2\right] - \lambda\,\mathrm{erfc}\left(\lambda\tau+\frac{z}{2\tau}\right)\right\},$$

$$\tau = \sqrt{\frac{t}{\mu\sigma}} \;, \quad \text{(A-4)}$$

whereby we find for the current density $j_\theta = \sigma E_\theta$

$$j_\theta = -\frac{M}{2\pi}\int_0^{\infty} \Phi(\lambda,z,t)\,\lambda^2 J_1(\lambda r)\, d\lambda \;, \quad \text{(A-5)}$$

with $\Phi(\lambda,z,t) = \mu\sigma\,\Phi'(\lambda,z,t)$.

This integral is computed numerically using the digital filter method of Fast Hankel Transforms (Johansen and Soerensen, 1979; Christensen, 1990) to give the current density shown in Figure 2a.

The contribution of the current to the measured magnetic field at the origin can be found from the formula for the magnetic field on the axis of a current loop

$$dH(\sigma,t) = j(\sigma,t,r,z)\, dr\, dz \times \frac{1}{2}\frac{r^2}{(r^2+z^2)^{3/2}} \;, \quad \text{(A-6)}$$

which using (A-5) can be written as

$$dH(\sigma,t,r,z) = dr\, dz\,\frac{M}{4\pi}\int_0^{\infty} \Phi(\lambda,z,t)\,\lambda^2\left\{\frac{r^2}{(r^2+z^2)^{3/2}}J_1(\lambda r)\right\} d\lambda \quad \text{(A-7)}$$

The contribution to the magnetic field, from a layer of thickness dz at depth equal to z is found by integrating (A-7) with respect to r from 0 to ∞. The integral only involves the term in the brackets {...}, and using Gradshteyn and Ryzhik (1965) 6.554.4 we find

$$dH(\sigma,t,z) = dz\,\frac{M}{4\pi}\int_0^{\infty} \Phi(\lambda,z,t)\exp(-\lambda z)\,\lambda^2\, d\lambda \quad \text{(A-8)}$$

$$= dz\,\frac{M}{4\pi}\int_0^{\infty}\left\{\frac{1}{\sqrt{\pi}\,\tau}\exp\left[-\left(\lambda\tau+\frac{z}{2\tau}\right)^2\right] - \lambda\,\mathrm{erfc}\left(\lambda\tau+\frac{z}{2\tau}\right)\right\}\lambda^2\, d\lambda \;.$$

First we find the integral

$$I_1 = \int_0^\infty \lambda^2 \exp\left[-(\lambda\tau + \frac{z}{2\tau})^2\right] d\lambda$$

$$= \exp\left[-\left(\frac{z}{2\tau}\right)^2\right] \int_0^\infty \lambda^2 \exp(-\lambda^2\tau^2 - \lambda z)\, d\lambda$$

(A-9)

$$= \exp\left[-\left(\frac{z}{2\tau}\right)^2\right] \left\{ -\frac{z/2}{2\tau^4} + \sqrt{\frac{\pi}{\tau^{10}}}\, \frac{2(z/2)^2 + \tau^2}{4} \exp\frac{(z/2)^2}{\tau^2} \operatorname{erfc}\frac{(z/2)}{\tau} \right\}$$

$$= \frac{1}{2\tau^3}\left[-u\exp(-u^2) + \sqrt{\pi}(u^2 + \tfrac{1}{2})\operatorname{erfc}(u)\right], \quad u = \frac{z}{2\tau},$$

where Gradshteyn and Ryzhik (1965) 3.462.7 has been used.

Then we calculate the second term first reducing by partial integration

$$I_2 = \int_0^\infty \lambda^3 \operatorname{erfc}(\lambda\tau + \frac{z}{2\tau})\, d\lambda$$

$$= \left[\tfrac{1}{4}\lambda^4 \operatorname{erfc}(\lambda\tau + \frac{z}{2\tau})\right]_0^\infty - \int_0^\infty \tfrac{1}{4}\lambda^4\left(-\frac{2}{\sqrt{\pi}}\right)\exp\left[-(\lambda\tau + \frac{z}{2\tau})^2\right] d\lambda$$

$$= \frac{\tau}{2\sqrt{\pi}} \exp\left[-\left(\frac{z}{2\tau}\right)^2\right] \frac{\partial^2}{\partial z^2} \int_0^\infty \lambda^2 \exp(-\lambda^2\tau^2 - \lambda z)\, d\lambda$$

$$= \frac{1}{16\sqrt{\pi}\,\tau^4} \exp(-u^2) \frac{\partial^2}{\partial u^2} \left\{ -u + \sqrt{\pi}(u^2 + \tfrac{1}{2})\exp(u^2)\operatorname{erfc}(u) \right\}$$

$$= \frac{1}{16\sqrt{\pi}\,\tau^4} \exp(-u^2) \frac{\partial}{\partial u} \left\{ -(2u^2 + 2) + \sqrt{\pi}(2u^2 + 3u)\exp(u^2)\operatorname{erfc}(u) \right\}$$

$$= \frac{1}{16\sqrt{\pi}\,\tau^4} \left\{ -(4u^3 + 10u) + \sqrt{\pi}(4u^4 + 12u + 3)\operatorname{erfc}(u) \right\}, \qquad \text{(A-10)}$$

where Gradshteyn and Ryzhik (1965) 3.462.7 has been used once more.

Combining the integrals I_1 and I_2 we find

$$dH(\sigma, t, z) = dz\, \frac{M}{4\pi} \frac{1}{16\tau^4} \left\{ \frac{2u}{\sqrt{\pi}}(2u^2 + 1)e^{-u^2} - (4u^4 + 4u^2 - 1)\operatorname{erfc}(u) \right\},$$

(A-11)

and thereby the Frechet kernel

$$\frac{\delta H}{\delta\sigma} = \frac{M}{4\pi} \frac{1}{16\sigma\tau^4} \left\{ \frac{2u}{\sqrt{\pi}}(2u^2 + 1)e^{-u^2} - (4u^4 + 4u^2 - 1)\operatorname{erfc}(u) \right\}$$

(A-12)

The above expression in the brackets is not numerically stable for large values of the argument u. For large values of u, we shall use the series expansion of the complementary error function (Abramowitz and Stegun, 1964, 7.1.23) and we find

$$\mathfrak{F}(u) = \left\{ \frac{2u}{\sqrt{\pi}}(2u^2 + 1)e^{-u^2} - (4u^4 + 4u^2 - 1)\operatorname{erfc}(u) \right\}$$

$$= \frac{1}{\sqrt{\pi}}(4u^3 + 2u)e^{-u^2} - (4u^4 + 4u^2 - 1)\frac{1}{\sqrt{\pi}\,u}e^{-u^2}$$

$$\times \left[1 - \frac{1}{2u^2} + \frac{1\cdot 3}{(2u^2)^2} - \frac{1\cdot 3\cdot 5}{(2u^2)^3} + \cdots\right]$$

$$= \frac{e^{-u^2}}{\sqrt{\pi}} \left\{ (4u^3 + 2u) - \frac{1}{u}(4u^4 + 4u^2 - 1)\left[1 - \frac{1}{2u^2} + \frac{1\cdot 3}{(2u^2)^2} - \frac{1\cdot 3\cdot 5}{(2u^2)^3} + \cdots\right] \right\}$$

$$= \frac{e^{-u^2}}{\sqrt{\pi}} \left\{ 4u^3 + 2u - 4u^3 - 4u + \frac{1}{u} + 2u + \frac{2}{u} - \frac{1}{2u^3} \right.$$

$$\left. -\frac{3}{u} - \frac{3}{u^3} + \frac{3}{4u^5} + \frac{15}{2u^3} + \frac{15}{2u^5} - \frac{15}{8u^7} - \cdots \right\}$$

$$= \frac{e^{-u^2}}{\sqrt{\pi}} \left\{ -\frac{7}{2u^3} + \frac{3}{4u^5} - \frac{1}{u}(4u^4 + 4u^2 - 1)\sum_{m=3}^{\infty}(-1)^m \frac{1\cdot 3\cdot 5\cdot \ldots \cdot(2m-1)}{(2u^2)^m} \right\}$$

(A-13)

from which it is seen that $\mathfrak{I}(u)$ decreases as $u^{-3}\exp(-u^{-2})$ for $u \to \infty$.

The Integrated Frechet Kernel

For the imaging algorithm, we need the integral over z of the Frechet kernel. Also for this integral an analytic expression can be found.

The partial integration rule gives us the formula

$$\int u^n \operatorname{erfc}(u)\, du = \frac{1}{n+1} u^{n+1}\operatorname{erfc}(u) + \frac{1}{n+1}\frac{2}{\sqrt{\pi}}\int u^{n+1}\exp(-u^2)\, du,$$

(A-14)

which we shall use in the following. We obtain

$$\hat{F}(\sigma, t, u) = \int F(\sigma, t, u)\, dz = \int F(\sigma, t, u)\, 2\tau\, du$$

$$= \frac{M}{4\pi}\frac{1}{8\sigma\tau^3} \int \left\{ \frac{2u}{\sqrt{\pi}}(2u^2 + 1)e^{-u^2} - (4u^4 + 4u^2 - 1)\operatorname{erfc}(u) \right\} du$$

$$= \frac{M}{4\pi}\frac{1}{8\sigma\tau^3} \left\{ \frac{2}{\sqrt{\pi}}\int (2u^3 + u)e^{-u^2}\, du - (\tfrac{4}{5}u^5 + \tfrac{4}{3}u^3 - u)\operatorname{erfc}(u) \right.$$

$$\left. - \frac{2}{\sqrt{\pi}}\int (\tfrac{4}{5}u^5 + \tfrac{4}{3}u^3 - u)e^{-u^2}\, du \right\}$$

$$= \frac{M}{4\pi}\frac{1}{8\sigma\tau^3} \left\{ -(\tfrac{4}{5}u^5 + \tfrac{4}{3}u^3 - u)\operatorname{erfc}(u) + \frac{2}{\sqrt{\pi}}\int (-\tfrac{2}{5}u^4 + \tfrac{1}{3}u^2 + 1)\, e^{-u^2}\, d(u^2) \right\}$$

$$= \frac{M}{4\pi}\frac{1}{8\sigma\tau^3} \left\{ -(\tfrac{4}{5}u^5 + \tfrac{4}{3}u^3 - u)\operatorname{erfc}(u) + \frac{2}{\sqrt{\pi}}\left[-\tfrac{2}{5}(-u^4 - 2u^2 - 2) + \tfrac{1}{3}(-u^2 - 1) - 1 \right] e^{-u^2} \right\}$$

$$= \frac{M}{4\pi}\frac{1}{120\sigma\tau^3} \left\{ \frac{2}{\sqrt{\pi}}(6u^4 + 7u^2 - 8)\, e^{-u^2} - u(12u^4 + 20u^2 - 15)\operatorname{erfc}(u) \right\},$$

(A-15)

where Gradshteyn and Ryzhik (1965) 2.322.1-2 have been used.

APPENDIX B
FINDING THE STEP RESPONSE FROM THE IMPULSE RESPONSE

Most transient data acquisition systems measure the rate of change of the magnetic flux through an induction coil for a repetitive alternating step-off in the source current, which is equivalent to the impulse response. However, the measured field quantity H' is not the pure impulse response. The response is modified through the finite turnoff time of the transmitter and due to the repetitive signal. Assuming the turnoff ramp and the turn-on ramp to be linear and neglecting contributions to the measured signal from transmitter signals earlier than the last turn-on, the measured response can be written in terms of the step response as

$$H'(t_i) = \frac{H(t_{i1}) - H(t_{i2})}{\Delta_{off}} - \frac{H(t_{i3}) - H(t_{i4})}{\Delta_{on}}, \qquad \text{(B-1)}$$

where

t_{i1} is the time since end of turnoff ramp,
t_{i2} is the time since start of turnoff ramp,
t_{i3} is the time since end of turn-on ramp,
t_{i4} is the time since start of turn-on ramp,
Δ_{off} is the turnoff ramp time, and
Δ_{on} is the turn-on ramp time.

H' is thus a linear function of the step response.

By expressing the step response as a linear combination of base functions f_j

$$H(t_i) = \sum_{1}^{M} A_j f_j(t_i) \qquad \text{(B-2)}$$

the measured response H' can be expressed as a linear function of the coefficients A_i. By solving this linear system of equations in a least squares sense, we can determine the coefficients A_i and thereby find the step response. This approach to the determination of the step response takes both the finite turnoff time and the run-on effect into account, and the actual uncertainties of the measured data can be incorporated in the solution of the linear system in the usual way.

Extensive numerical experiments have led to a solution to the above problem taking ln(t) as variable instead of t, and the quotient between the step response of the measurements and the step response of a homogeneous halfspace as dependent variable. The linearity of the problem is preserved by these transformations. The base functions are chosen as

$$f_j(x) = \frac{1}{1 + \exp\left[-b\cdot(x - x_j)\right]} \qquad \text{(B-3)}$$

where the x_j are chosen with a uniform sampling density of 0.5e in the interval from $\ln(t_i)$ to $\ln(t_N)$, where t_i and t_N are the earliest and the latest time of measurement. The parameter b is chosen equal to 6.

Generally, the above algorithm works well, but it does break down in certain cases. Sometimes the all-time apparent resistivity found from the step response will display a rapidly increasing branch for late times without any justification in the measured data or the general geological background. This means that sometimes the apparent resistivity transform must be weeded out by hand-slowing down the inversion process and impairing the automation of the procedure.

Three pieces of information should be incorporated in a future improvement of the algorithm for finding the step response. Firstly, the value of the normalized step-response at time zero is unity. Secondly, the late time asymptotic behavior of the step response is known. For a 1D earth model, the step response decays as $^{-3/2}$. Thirdly, the frequency content of the step response, and thereby the possible rate of change of the response, is restricted to lower and lower frequencies as time increases. Preferably, the base functions should be chosen to automatically fulfill these three requirements. The above procedure incorporates the second of the requirements, in that the base functions automatically approach a constant for the quotient between the step response of the measurements and the step response of a homogeneous halfspace as time goes to infinity.

With 60 measurements of H' distributed over 3 decades in time, it takes less than 0.5s to find the step response on a 1 Mflop computer. The mean fit to the measured H' field is usually of the order of a few percent. When doing the imaging on the step responses calculated from the impulse response, the models become slightly more noisy than when using the exact step response, but the difference is small.